

Characteristics of Two-episode Emission Patterns in *Fermi* Long Gamma-Ray Bursts

Lin Lan¹, Hou-Jun Lü^{*1}, Shu-Qing Zhong¹, Hai-Ming Zhang¹, Jared Rice², Ji-Gui Cheng¹,
Shen-Shi Du¹, Long Li¹, Jie Lin¹, Rui-Jing Lu¹, and En-Wei Liang¹

ABSTRACT

Two-episode emission components separated by quiescent gaps in the prompt emission of gamma-ray bursts (GRBs) have been observed in the *Swift* era, but there is a lack of spectral information due to the narrow energy band of the *Swift*/Burst Alert Telescope. In this paper, a systematic analysis of the spectral and temporal properties of the prompt emission of 101 *Fermi*/Gamma-ray Burst Monitor detected long GRBs show the existence of two-episode emission components in the light curves, with quiescent times of up to hundreds of seconds. We focus on investigating the differences of those two emission episodes. We find that the light curves of the two emission components exhibit different behavior, e.g., a soft emission component that either precedes or follows the main prompt emission or that the intensity of the two emission episodes are comparable with each other. No statistically significant correlation in the duration of the two emission episodes can be claimed. We define a new parameter ε as the ratio of the peak flux of the first and second emission episodes and find that a higher ε corresponds to a larger fluence. The preferred spectral model in our analysis is a cutoff power-law model for most GRBs. The distribution of E_p for episodes I and II range from tens of keV to 1000 keV with a lognormal fit and there are no significant differences between them. Moreover, we do not find significant relationships between ε and E_p for the two emission episodes. Those results suggest that these two-episode emission components likely share the same physical origin.

Subject headings: gamma-ray burst: general- methods: statistical

1. Introduction

Quantitatively, the duration of a burst is usually defined by T_{90} which is the time interval between 5% and 95% of the total fluence for a given detector. Phenomenologically, gamma-ray bursts (GRBs) are classified into two categories, long and short, with a division line at the observed

¹Guangxi Key Laboratory for Relativistic Astrophysics, Department of Physics, Guangxi University, Nanning 530004, China; lhj@gxu.edu.cn

²Department of Physics and Astronomy, University of Nevada Las Vegas, Las Vegas, NV 89154, USA

duration $T_{90} \sim 2$ seconds in the CGRO/BATSE era (Kouveliotou et al. 1993). The bimodal distribution of T_{90} , on the other hand, together with information about host galaxies and afterglow, suggests that long GRBs are related to the deaths of massive stars (Narayan et al. 1992; Woosley 1993; MacFadyen & Woosley 1999; Berger et al. 2005; Tanvir et al. 2005; Fruchter et al. 2006; Zhang 2006), and short GRBs are associated with the merger of two compact stellar objects, such as the merger of two neutron stars (Paczynski 1986; Eichler et al. 1989), or the merger of a neutron star and a black hole (Paczynski 1991). These progenitors result in the immediate formation of a black hole (or magnetar) that powers a relativistic jet, whose radiation can be observed if the jet is pointing toward the direction of the observer from within an optically thin region (Usov 1992; Woosley 1993; Thompson 1994; Dai & Lu 1998; Popham et al. 1999; Zhang & Mészáros 2001; Metzger et al. 2008; Lei et al. 2013; Lü & Zhang 2014; Liu et al. 2017). The prompt emission and afterglow emission are usually considered to be emission from internal shocks (ejecta internally dissipating energy) and external shocks (ejecta interacting with a circum-burst medium), respectively (Paczynski 1986; Shemi & Piran 1990; Mészáros & Rees 1997; Kumar 1999; Kumar & Zhang 2015).

Moreover, the duration of the prompt emission can reflect the activity of the GRB central engine (Zhang et al. 2016). However, Qin et al. (2013) found that the bimodal T_{90} distribution of *Fermi*/Gamma-ray Burst Monitor (GBM) data is significantly different from the distributions found in both *BeppoSAX*/GRBM and *Swift*/Burst Alert Telescope (BAT) data. They also found differences in the measured T_{90} in different energy bands for the same burst. These findings indicate that T_{90} is significantly affected by instrumental selection effects and is energy-dependent. On the other hand, the long, soft extended emission tails (Della Valle et al. 2006; Fynbo et al. 2006; Gal-Yam et al. 2006; Gehrels et al. 2006), the internal plateau (Troja et al. 2007; Lyons et al. 2010; Rowlinson et al. 2010, 2013; Lü et al. 2015), and the erratic, bright X-ray flares observed with *Swift* /BAT and the X-ray Telescope (XRT) challenge the simple classification based on the T_{90} criterion (Barthelmy et al. 2005; Nousek et al. 2006; Zhang et al. 2006; Perley et al. 2009; Lü et al. 2010; Zhang et al. 2014; Gao et al. 2017). In particular, the X-ray flares and internal plateaus observed in XRT are very difficult to interpret with the external shock model. The late activities of the GRB central engine (Burrows et al. 2005; Fan & Wei 2005; King et al. 2005; Dai et al. 2006; Zhang et al. 2006) show that internal dissipation is more favorable in explaining these phenomena. This observational evidence suggests that the activity of the central engine of GRBs does not stop for longer than 10^4 s.

Observational data indicate that at least $\sim (9 - 15)\%$ of GRB prompt emission signatures are composed of two or more emission episodes with a quiescent time that may be extremely long, e.g., up to ~ 100 s in the rest frame (Koshut et al. 1995; Lazzati 2005; Burlon et al. 2008; Bernardini et al. 2013; Hu et al. 2014). Considering the case of two-episode emission components, a single prompt emission light-curve pattern resembling a soft emission (precursor) does not exist prior to the main prompt event (Koshut et al. 1995; Lazzati 2005; Burlon et al. 2008; Hu et al. 2014), nor does a soft emission (similar to extended emission) after the main prompt event, or the emissions

from those two episodes are comparable with each other. Beyond that, some events observed by *Swift*/BAT were triggered twice with a temporal separation of hundreds of seconds, called double bursts (e.g., GRB 110709B; Zhang et al.2012; Hu et al. 2014; Liu et al. 2014). On the other hand, in previous studies, the spectral analysis of those two-episode emissions used the hardness ratio to roughly compare the spectral properties. However, this cannot reflect the intrinsic properties of the spectra due to the narrow energy band of *Swift*/BAT (Barthelmy et al. 2005). Therefore, measuring the peak energy (E_p) of spectra is an important aspect of understanding the hardness of the two-episode emissions and determining if there are intrinsic relationships and evolution between them.

It is possible to diagnose the spectral properties of those multiepisode emissions thanks to the *Fermi* satellite, which provides an unprecedented spectral coverage over 7 orders of magnitude in energy (from ~ 8 keV to ~ 300 GeV). *Fermi* includes two instruments. One is the GBM containing 12 sodium iodide (NaI) detectors that cover an energy range from 8 keV to 1 MeV and two bismuth germanate (BGO) scintillation detectors that are sensitive to higher energies between 200 keV and 40 MeV (Meegan et al. 2009). The other is the Large Area Telescope (LAT) with an energy coverage from 20 MeV to 300 GeV (Atwood et al. 2009). Observationally, not all GRBs detected by GBM are seen with high-energy emission in LAT and only a few bursts have exhibited high-energy emission over the last 9 years (Ackermann et al.2013; Vianello et al. 2015). Due to the narrow energy band of *Swift* /BAT, it is often not possible to derive a full spectrum, and the best fit is a simple power-law (PL) model. Nevertheless, *Fermi*/GBM covers a broad energy band, and the peak energy (E_p) of the spectrum of most GRB prompt emission episodes can be derived by invoking a Band function, or cutoff power-law (CPL) model. Several questions regarding these multiepisode emission of prompt emission GRBs are worthy of discussion. Does a spectral evolution exist between the emission episodes? Are there correlations between observed parameters for the episodes? Our goal is to systematically analyze the GRB data observed by *Fermi*/GBM since its operations began in 2008, aiming to address the abovementioned problems in GRB prompt emission. In this paper, we focus on a comprehensive analysis of the GRBs detected by GBM, and present a two-episode emission GRB catalog with our spectral and temporal analysis. Our data reduction and analysis methods are presented in §2 and the analysis results are reported in §3. The conclusions and a discussion are presented in §4.

2. Data reduction and sample selection

2.1. Light-curve extraction

Fermi, a high-energy γ -ray satellite, has operated for more than 9 years since it was launched in 2008. There are three different types of signals from each of the 14 GBM detectors: CTIME,

CSPEC, and TTE¹. We do not use CTIME data and CSPEC data in our analysis due to the fixed time resolution of 64 ms and 1.024 s, but select the TTE data that include individual photons arriving with time and energy tags. Moreover, we can select any time resolution bin size to perform our spectral and temporal analysis.

We download the original GBM data (12 NaI and 2 BGO detectors), as well as LAT data of GRBs from the public science support center at the official *Fermi* website². We choose the brightest detector among NaI and BGO to do the analysis, respectively, because the brightest detector has a minimum angle between the incident photon and the normal direction of the detector. Based on the standard `heasoft` tools (version 6.19) and the *Fermi ScienceTools* (v10r0p5), a *Python* code was developed to extract the energy-dependent light curves and time-dependent spectra using the spectral source package *gtBurst*³. We employ the Bayesian Block algorithm to identify the light curves. Please refer to our latest paper (Lu et al. 2017) for more details on data analysis with the Bayesian Block algorithm. Several points need to be cautioned: firstly, we extract the light curve with a time bin of 128 ms to identify a possible signal in different energy bands in the time interval [-100, 300] s, and we adopt 10 control blocks for picking up a weaker signal in our analysis. Then, we extract the light curve again by adopting a 64 ms time bin instead of the 128 ms time bin, if a possible Bayesian block can be identified. The motivation for using a 64 ms time bin by running again instead of a 128 ms time bin is to find microstructure in the light curves, in particular, in the soft precursor emission, which may have a short duration. Also, a signal-to-noise ratio (S/N) of at least 3σ is believed to be a true signal⁴. Finally, we calculate the duration (5% and 95% of the total photons for each episode) of the bursts within the energy band 8 - 1000 keV. In Table 1, we summarize our results and indicate $T_{E,I}$ and $T_{E,II}$ as the duration of the first and second emission episodes.

2.2. Sample selection criteria

As of August 2017, we have extracted the light curves of 2059 GRBs that were detected by *Fermi* /GBM. The LAT light curve is also extracted if the LAT data are available. The full data set includes 1764 long GRBs and 295 short GRBs. There are three criteria adopted for our sample selection. First, the prompt emission must have two emission episodes with the quiescent time

¹The continuous time (CTIME) data include eight energy channels and have a finer time resolution of 64 ms. The continuous spectroscopy (CSPEC) data include 128 energy channels, and a time resolution of 1.024 s. The time-tagged event (TTE) data consist of individual detector events, each tagged with arrival time, energy (128 channels), and detector number (Paciesas et al. 2012).

²<http://fermi.gsfc.nasa.gov/ssc/data/>.

³<http://sourceforge.net/projects/gtburst/>.

⁴In order to obtain the arrival time of different energy photons, we separate the NaI and BGO detectors into two energy bands, respectively, e.g., [8, 50] keV and [50, 1000] keV for NaI; [250, 1000] keV and >1000 keV for BGO.

between these episodes being longer than 5 s. Second, the S/N ratio of the emission episodes should be greater than 3σ . Third, we focus on long GRBs that have a main prompt emission duration longer than 5 s. There are 101 GRBs that satisfy our criteria up to 2017 August, 4 of which have a measured redshift, e.g., GRBs 091208B, 100615A, 140512A, and 151027A. It also includes 6 GRBs detected by LAT, e.g. GRBs 090328, 100116A, 121225B, 130821A, 150118B, and 150523A.

2.3. Spectrum extraction

The background spectrum from the GBM data are extracted from two time intervals: before the first emission episode and after the last emission episode, and are modeled with a polynomial function. XSPEC is used to perform spectral fits for each episode. The motivation of this work is focused on comparing the difference between those two episodes' emission. So that, in our spectral analysis, we only perform the time-integrated spectral fits even though the spectral evolution may exist for each episode emission. The statistic χ^2 is adopted to judge the goodness of the spectral fits. In our analysis a Band function model (Band et al. 1993), a widely used phenomenological model, is invoked as the primary model and is written as

$$N_{\text{Band}}(E) = B(E) = A \begin{cases} (\frac{E}{100 \text{ keV}})^\alpha \exp(-\frac{E}{E_0}), & E < (\alpha - \beta)E_0 \\ [\frac{(\alpha - \beta)E_0}{100 \text{ keV}}]^{\alpha - \beta} \exp(\beta - \alpha) (\frac{E}{100 \text{ keV}})^\beta, & E \geq (\alpha - \beta)E_0 \end{cases} \quad (1)$$

where A is the normalization of the spectrum, α and β are the low and high-energy photon spectral indices, respectively; E_0 is the break energy of the spectrum, and the peak energy (E_p) of the spectrum is related to E_0 through

$$E_p = (2 + \alpha)E_0. \quad (2)$$

Alternatively, if the Band function model is not good enough to fit the data, a CPL or a simple PL model are adopted, which can be written as

$$N_{\text{CPL}}(E) = A \cdot E^{-\alpha} \exp(-\frac{E}{E_p}), \quad (3)$$

$$N_{\text{PL}}(E) = A \cdot E^{-\alpha}. \quad (4)$$

The examples of spectral fitting in our sample are shown in Figure 1, and the fitting results for each episode are shown in Table 1, The peak energy and PL indices of the spectrum of the first and second emission episodes are indicated as $E_{p,\text{I}}$ and $E_{p,\text{II}}$, and as α_{I} and α_{II} , respectively.

3. Results

3.1. Light curves, duration, and quiescent time

Phenomenologically, the light curves of those two-episode emission components show different behaviors, e.g., a soft emission component prior to (40 out of 101) or following (7 out of 101) the main prompt emission,⁵ or the intensity of the two emission episodes are comparable with each other (54 out of 101). Three examples of such light-curve patterns are shown in Figure 1.

Based on the Bayesian block method, we calculate the duration of each emission episode, (T_{episode}), and show the distribution of T_{episode} in Figure 2(a), as well as the distribution of quiescent time⁶ ($T_{\text{quiescent}}$) between the two emission episodes in Figure 2(b). The duration of the two emission episodes and the quiescent time follow a lognormal distribution with $\log T_{\text{episode,I}} = (1.09 \pm 0.02)$ s, $\log T_{\text{episode,II}} = (1.16 \pm 0.05)$ s, and $\log T_{\text{quiescent}} = (1.44 \pm 0.05)$ s, respectively. The maximum and minimum quiescent times in our sample are 223.36 s for GRB 131108A and 5.42 s for GRB 091208B, respectively. Bernardini et al. (2013) proposed that the precursor and prompt emission arise from the accretion of matter onto the surface of the magnetar, and a longer quiescent time of the two emission episodes should correspond to a higher intensity for the second emission episode. However, we do not find any correlations between $T_{\text{quiescent}}$ and $T_{\text{episode,I/II}}$. This suggests that the physical origin of the two emission episodes may not be related to the accretion physics. Moreover, it may introduce constraints on the proposed models that are invoked for interpreting the two emission episodes.

In order to identify the brightness of each episode from the same burst, we define one dimensionless parameter, the relative factor ε , which is the ratio of the 1-s peak flux between the two emission episodes within 8 keV - 40 MeV,

$$\varepsilon = \frac{F_{e,\text{I}}}{F_{e,\text{II}}}, \quad (5)$$

where $F_{e,\text{I}}$ and $F_{e,\text{II}}$ are the 1 s peak flux of the first and second episodes, respectively. We extract the 1 s peak flux of each episode based on the spectra and present them in Table 1. Figure 3 shows the distribution of ε in our sample. Figures 4(a) and (b) present the distributions of fluence for episodes I and II in our sample, which follow a lognormal distribution with $\log S_{e,\text{I}} = (-5.21 \pm 0.04)$ erg cm⁻² and $\log S_{e,\text{II}} = (-5.24 \pm 0.05)$ erg cm⁻². Interestingly, we found that larger ε (the first emission episode brighter) corresponds to a higher fluence, see Figure 4(c).

⁵Here, we define the peak flux of each episode to indicate the strength of each emission episode.

⁶The definition of quiescent time is the duration between the end of the first episode and the beginning of the second episode.

3.2. Spectral properties

Although the Band function (Band) is our primary spectral model for fitting the data and the χ^2 statistic is good enough, the high-energy index β cannot be constrained very well. The values of β have large error bars and are much less than the typical value -2.3 for most GRBs. There are no significant differences in the fits with a Band model as compared with the CPL model, but the CPL model has fewer independent parameters. The χ^2 value of the PL model fits is much larger than that of the CPL models. Beyond that, we also try to invoke the blackbody (BB) model or more free parameter multi-component models to fit the spectra (e.g., BB+Band, BB+CPL, and BB+PL), but the temperature of BB is very difficult to constrain. Therefore, the preferred spectral model in our analysis is the CPL model for most GRBs, except for two episodes that are modeled well by a Band function, e.g. the second episode of GRB 150330A (bn150330828) and the first episode of GRB 170409A (bn170409112). On the other hand, LAT data are also presented for six GRBs in our sample. By considering the contributions of LAT data for spectral analysis in the two emission episodes, the first and second episodes of GRBs 121225B, 130821A, and 150118B are well modeled by a Band function and a CPL model, respectively. Moreover, the first emission episodes of GRBs 090328 and 150523 are well modeled by a Band function with an extra CPL or PL components, as well as the second episode emission of GRB 100116A with the Band function model. The spectral parameters derived from our fits are reported in Table 1.

However, the origin of high-energy GeV photons remains under debate, as well as whether keV - MeV and GeV photons share the same physical origin. Thus, by ignoring the contribution of LAT/LLE data, we reanalyze the spectra of those six GRBs with LAT detections, and find that the CPL model is favored to perform spectral fits. The top panels of Figure 5 ((a) and (b)) show the distributions of $E_{p,I}$ and $E_{p,II}$, the peak energy of the spectra for the first and second emission episodes. The $E_{p,I}$ and $E_{p,II}$ distributions range from tens of keV to 1000 keV. Both of them are followed by lognormal distributions with peaks at $\log E_{p,I} = (2.31 \pm 0.02)$ keV and $\log E_{p,II} = (2.22 \pm 0.03)$ keV, respectively. Similarly, the bottom panels of Figure 5 ((a) and (b)) show the distributions of α_I and α_{II} , the spectral index for the first and second episodes' emission. The distributions are also normal with mean values of $\alpha_I = 0.9 \pm 0.02$ and $\alpha_{II} = 1.15 \pm 0.03$. From a statistical point of view, the peak energy of the first emission episode appear to be slightly harder than that of the second episode. However, a statistical test using the method proposed by Ashman et al. (1994) yields $P_{ks} = 0.083$, which indicates that they cannot be absolutely distinguished as arising from a different population.

In order to test whether the brighter emission episode corresponds to a higher E_p of the spectrum for the same burst, Figure 5 (c) shows the distributions of $E_{p,I} - E_{p,II}$ and $\alpha_I - \alpha_{II}$. We do not find a significant difference between higher (or lower) ε and harder (or softer) E_p . A similar result holds for the photon index α of spectral fits.

4. Conclusions and Discussion

We have presented a comprehensive temporal and spectral analysis for two-episode prompt emission of GRB data observed with *Fermi*/GBM during 9 years of operation, where the two emission episodes are separated by a quiescent time of up to hundreds of seconds. We studied the possibility of the existence of significant differences between the two emission episodes. Our results are summarized as follows:

- We find that the light curves of 101 long GRBs with two-episode emission components show different behavior, e.g., a soft emission component prior to (40 out of 101) or following (7 out of 101) the main prompt emission, or that the intensity of those two emission episodes are comparable (54 out of 101).
- The distributions of episodes I, II, and the quiescent time are normal. The maximum and minimum quiescent times in our sample are 223.36 s for GRB 131108A and 5.42 s for GRB 091208B, respectively. There are no correlations between $T_{\text{quiescent}}$ and $T_{\text{episode,I/II}}$, but there is a possible correlation between ε and fluence, e.g., the brighter episode corresponds to higher fluence.
- The preferred spectral model in our analysis is the CPL model for most GRBs. The distribution of E_p for episodes I and II are lognormal and range from tens of keV to 1000 keV. Moreover, we do not find significant differences between higher (or lower) ε and harder (or softer) E_p . This suggests that the two-episode emission components may share the same physical origin.

Based on our analysis, about 5% of long GRBs include two-episode emission components for the same burst in the *Fermi* era (101 out of 1764). This fraction is less than that in the *Swift* era ($\sim 9\%$, Koshut et al. 1995; Lazzati 2005; Burlon et al. 2008; Bernardini et al. 2013; Hu et al. 2014). This difference may be related to the different method we used to search for the signal or the fact that the sensitivity of different instruments with different trigger energy maybe exhibit differences. On the other hand, there are two ways by which such two-episode emission may be caused in two ways: either the emission is continuous but the signal in the quiescent time is too weak to be detected by current γ -ray detectors, e.g. the tip-of-the-iceberg effect in Lü et al. 2014 or the emission is intrinsic and no signal exists during the quiescent time (Hu et al. 2014).

Lu et al. (2012) showed either an evolution from hard to soft for single-pulse or multipulse GRBs detected by *Fermi*/GBM or intensity tracking behavior. In order to test whether the soft first emission episode is the subemission of the second one, we compare the peak energy of the first emission episode with the second. In our analysis, we do not find a difference in the E_p distribution between the two episodes, indicating that the first episode is not likely to be subemission of the second episode.

From a theoretical point of view, the physical interpretation of these two-episode emissions

remains an open question. One possible interpretation is that when a jet propagates within the stellar envelope (Ramirez-Ruiz et al. 2002; Lazzati & Begelman 2010; Nakar & Piran 2017) the wasted energy of the jet is recycled into a high pressure cocoon surrounding the relativistic jet (Ramirez-Ruiz et al. 2002; Lazzati & Begelman 2005). Wang & Mészáros (2007) proposed that the first soft emission is produced by the jet bow shock, the quiescent time is due to the pressure drop ahead of the jet head after it reaches the stellar surface, and the second emission episode is from a relativistic jet that is accelerated by a rarefaction wave. Lipunova et al. (2009) proposed two steps in the collapse of the progenitor star, i.e., it first collapses to a neutron star (soft emission) and then into a black hole (main emission). These models predict that the time gap is only tens of seconds and the first soft emission has a thermal spectrum. Even a small fraction of the time gap for our samples ranges over tens of seconds, but the lack of a thermal component for spectra from observations is not consistent with the prediction of the above models. Alternatively, the multi-episode nature of these events may be directly related to central engine activity (Ramirez-Ruiz et al. 2001) similar to a newly born magnetar as a the central engine of GRBs, the precursor and the prompt emission arise from the accretion of matter onto the surface of the magnetar (Bernardini et al. 2013). However, it is difficult to interpret the case of main emission followed by a soft emission. For the case of soft emission at a later time, several models have been proposed, e.g., the collapse of a rapidly rotating stellar core leading to fragmentation (King et al. 2005), fragmentation in the accretion disk (Perna et al. 2006), or a magnetic barrier around the accretor (Proga & Zhang 2006).

On the other hand, some possible interpretations of the double bursts are that a single GRB is located behind a foreground galaxy and is gravitationally lensed before reaching the detectors, or the jet precesses in a black hole hyper-accretion system (Zhang et al. 2012; Liu et al. 2014). These interpretations require more observational data and information about the host galaxy to be identified. Moreover, there are only four GRBs, GRBs 091208B, 100615A, 140512A, and 151027A, with measured redshifts in our sample. Due to a lack of host galaxy information and optical observations in our sample (leading to a lack of redshift measurements), one cannot measure an intrinsic peak luminosity and isotropic energy for the two emission episodes in order to constrain the theoretical model. More observational data are needed in the future to present a unified picture and interpret prompt emission light curves.

We acknowledge the use of the public data from the *Fermi* data archive. This work is supported by the National Basic Research Program (973 Programme) of China 2014CB845800, the National Natural Science Foundation of China (grant Nos. 11603006, 11851304, 11533003, 11363002, and U1731239), the Guangxi Science Foundation (grant Nos. 2017GXNSFFA198008, 2016GXNS-FCB380005, and AD17129006). The One-Hundred-Talents Program of Guangxi colleges, the high level innovation team and outstanding scholar program in Guangxi colleges, Scientific Research Foundation of Guangxi University (grant No. XGZ150299), and special funding for Guangxi distinguished professors (Bagui Yingcai and Bagui Xuezhe).

REFERENCES

- Ackermann, M., Ajello, M., Asano, K., et al. 2013, *ApJS*, 209, 11
- Ashman, K. M., Bird, C. M., & Zepf, S. E. 1994, *AJ*, 108, 2348
- Atwood, W. B., Abdo, A. A., Ackermann, M., et al. 2009, *ApJ*, 697, 1071
- Band, D., Matteson, J., Ford, L., et al. 1993, *ApJ*, 413, 281
- Barthelmy, S. D., Barbier, L. M., Cummings, J. R., et al. 2005, *Space Sci. Rev.*, 120, 143
- Berger, E., Price, P. A., Cenko, S. B., et al. 2005, *Nature*, 438, 988
- Bernardini, M. G., Campana, S., Ghisellini, G., et al. 2013, *ApJ*, 775, 67
- Burlon, D., Ghirlanda, G., Ghisellini, G., et al. 2008, *ApJ*, 685, L19
- Burrows, D. N., Romano, P., Falcone, A., et al. 2005, *Science*, 309, 1833
- Dai, Z. G., & Lu, T. 1998, *A&A*, 333, L87
- Dai, Z. G., Wang, X. Y., Wu, X. F., & Zhang, B. 2006, *Science*, 311, 1127
- Della Valle, M., Chincarini, G., Panagia, N., et al. 2006, *Nature*, 444, 1050
- Eichler, D., Livio, M., Piran, T., & Schramm, D. N. 1989, *Nature*, 340, 126
- Fan, Y. Z., & Wei, D. M. 2005, *MNRAS*, 364, L42
- Fruchter, A. S., Levan, A. J., Strolger, L., et al. 2006, *Nature*, 441, 463
- Fynbo, J. P. U., Watson, D., Thöne, C. C., et al. 2006, *Nature*, 444, 1047
- Gal-Yam, A., Fox, D. B., Price, P. A., et al. 2006, *Nature*, 444, 1053
- Gao, H., Ren, A.-B., Lei, W.-H., et al. 2017, *ApJ*, 845, 51
- Gehrels, N., Norris, J. P., Barthelmy, S. D., et al. 2006, *Nature*, 444, 1044
- Hu, Y.-D., Liang, E.-W., Xi, S.-Q., et al. 2014, *ApJ*, 789, 145
- King, A., O’Brien, P. T., Goad, M. R., et al. 2005, *ApJ*, 630, L113
- Koshut, T. M., Kouveliotou, C., Paciesas, W. S., et al. 1995, *ApJ*, 452, 145
- Kouveliotou, C., Meegan, C. A., Fishman, G. J., et al. 1993, *ApJ*, 413, L101
- Kumar, P. 1999, *ApJ*, 523, L113
- Kumar, P., & Zhang, B. 2015, *Phys. Rep.*, 561, 1

- Lü, H.-J., Liang, E.-W., Zhang, B.-B., & Zhang, B. 2010, *ApJ*, 725, 1965
- Lü, H.-J., & Zhang, B. 2014, *ApJ*, 785, 74
- Lü, H.-J., Zhang, B., Lei, W.-H., Li, Y., & Lasky, P. D. 2015, *ApJ*, 805, 89
- Lü, H.-J., Zhang, B., Liang, E.-W., Zhang, B.-B., & Sakamoto, T. 2014, *MNRAS*, 442, 1922
- Lazzati, D. 2005, *MNRAS*, 357, 722
- Lazzati, D., & Begelman, M. C. 2010, *ApJ*, 725, 1137
- Lazzati, D., & Begelman, M. C. 2005, *ApJ*, 629, 903
- Lei, W.-H., Zhang, B., & Liang, E.-W. 2013, *ApJ*, 765, 125
- Lipunova, G. V., Gorbovskoy, E. S., Bogomazov, A. I., & Lipunov, V. M. 2009, *MNRAS*, 397, 1695
- Liu, T., Gu, W.-M., & Zhang, B. 2017, *NewAR*, 79, 1
- Liu, T., Sun, M.-Y., Hou, S.-J., et al. 2014, *Chinese Physics Letters*, 31, 119801
- Lu, R.-J., Du, S.-S., Cheng, J.-G., et al. 2017, [arXiv:1710.06979](https://arxiv.org/abs/1710.06979)
- Lu, R.-J., Wei, J.-J., Liang, E.-W., et al. 2012, *ApJ*, 756, 112
- Lyons, N., O’Brien, P. T., Zhang, B., et al. 2010, *MNRAS*, 402, 705
- Mészáros, P., & Rees, M. J. 1997, *ApJ*, 476, 232
- MacFadyen, A. I., & Woosley, S. E. 1999, *ApJ*, 524, 262
- Meegan, C., Lichti, G., Bhat, P. N., et al. 2009, *ApJ*, 702, 791-804
- Metzger, B. D., Quataert, E., & Thompson, T. A. 2008, *MNRAS*, 385, 1455
- Nakar, E., & Piran, T. 2017, *ApJ*, 834, 28
- Narayan, R., Paczynski, B., & Piran, T. 1992, *ApJ*, 395, L83
- Nousek, J. A., Kouveliotou, C., Grupe, D., et al. 2006, *ApJ*, 642, 389
- Paciesas, W. S., Meegan, C. A., von Kienlin, A., et al. 2012, *ApJS*, 199, 18
- Paczynski, B. 1986, *ApJ*, 308, L43
- Paczynski, B. 1991, *Acta Astron.*, 41, 257
- Perley, D. A., Metzger, B. D., Granot, J., et al. 2009, *ApJ*, 696, 1871
- Perna, R., Armitage, P. J., & Zhang, B. 2006, *ApJ*, 636, L29

- Popham, R., Woosley, S. E., & Fryer, C. 1999, *ApJ*, 518, 356
- Proga, D., & Zhang, B. 2006, *MNRAS*, 370, L61
- Qin, Y., Liang, E.-W., Liang, Y.-F., et al. 2013, *ApJ*, 763, 15
- Ramirez-Ruiz, E., Celotti, A., & Rees, M. J. 2002, *MNRAS*, 337, 1349
- Ramirez-Ruiz, E., Merloni, A., & Rees, M. J. 2001, *MNRAS*, 324, 1147
- Rowlinson, A., O’Brien, P. T., Metzger, B. D., Tanvir, N. R., & Levan, A. J. 2013, *MNRAS*, 430, 1061
- Rowlinson, A., O’Brien, P. T., Tanvir, N. R., et al. 2010, *MNRAS*, 409, 531
- Shemi, A., & Piran, T. 1990, *ApJ*, 365, L55
- Tanvir, N. R., Chapman, R., Levan, A. J., & Priddey, R. S. 2005, *Nature*, 438, 991
- Thompson, C. 1994, *MNRAS*, 270, 480
- Troja, E., Cusumano, G., O’Brien, P. T., et al. 2007, *ApJ*, 665, 599
- Usov, V. V. 1992, *Nature*, 357, 472
- Vianello, G., Omodei, N., Piron, F., & Razzaque, S. 2015, 3rd Annual Conference on High Energy Astrophysics in Southern Africa (HEASA2015), 35
- Wang, X.-Y., & Mészáros, P. 2007, *ApJ*, 670, 1247
- Woosley, S. E. 1993, *ApJ*, 405, 273
- Zhang, B.-B., Burrows, D. N., Zhang, B., et al. 2012, *ApJ*, 748, 132
- Zhang, B.-B., Zhang, B., Murase, K., Connaughton, V., & Briggs, M. S. 2014, *ApJ*, 787, 66
- Zhang, B. 2006, *Nature*, 444, 1010
- Zhang, B., Fan, Y. Z., Dyks, J., et al. 2006, *ApJ*, 642, 354
- Zhang, B., Lü, H.-J., & Liang, E.-W. 2016, *Space Sci. Rev.*, 202, 3
- Zhang, B., & Mészáros, P. 2001, *ApJ*, 552, L35

Table 1. Results of the temporal and spectral analysis of 101 GRBs in our sample.

Trigger ID	$T_{E,I}^a$ (s)	$F_{p,I}^b$ (10^{-7} erg cm $^{-2}$ s $^{-1}$)	$E_{p,I}^c$ (keV)	α_I^d	(χ^2 /dof)	T_q^e (s)	$T_{E,II}^a$ (s)	$F_{p,II}^b$ (10^{-7} erg cm $^{-2}$ s $^{-1}$)	$E_{p,II}^c$ (keV)	α_{II}^d	(χ^2 /dof)
bn080724401	8.77	6.44±3.94	103.25±13.76	0.80±0.09	257/237	10.54	1.60	7.81±5.64	114.58±5.35	0.50±0.04	241/237
bn081009140	9.15	73.02±2.15	53.18±1.75	1.11±0.03	260/233	27.86	12.80	9.96±5.71	18.8±2.07	1.34±0.14	256/238
bn090131090	9.66	21.66±2.03	48.79±3.75	0.92±0.07	267/236	13.23	16.26	12.39±2.45	209.98±29.77	1.38±0.04	242/237
bn090328401	29.82	14.18±5.80	767.59±78.09	0.98±0.03	253/237	23.23	4.29	4.16±0.09	64.84±26.99	0.85±0.34	247/237
bn090524346	16.32	12.98±5.52	99.43±12.82	0.76±0.10	220/239	27.01	6.53	3.18±0.48	81.34±20.95	1.29±0.15	249/239
bn090529564	2.29	17.68±7.27	215.96±47.37	0.82±0.11	270/238	6.62	2.80	14.00±4.99	198.33±30.37	0.91±0.07	262/239
bn090717034	13.18	15.8±4.29	186.17±4.73	1.07±0.01	326/237	32.08	14.27	5.97±5.85	91.25±16.78	0.71±0.14	241/238
bn091030828	6.91	8.29±0.36	110.8±13.43	0.12±0.13	245/238	10.67	20.93	29.02±17.10	949.52±152.99	1.01±0.04	266/238
bn091120191	39.68	18.00±3.61	181.36±20.12	1.16±0.05	232/239	9.17	5.89	4.19±0.32	79.58±15.96	1.00±0.14	254/239
bn091123298	18.24	4.93±1.46	154.59±21.22	0.57±0.10	234/240	143.47	20.35	4.84±0.33	256.32±76.94	1.38±0.09	222/240
bn091208410	3.68	4.01±0.19	101.4±30.94	1.13±0.16	275/237	5.42	3.58	15.45±2.39	158.02±27.19	1.12±0.08	259/237
bn100116897	3.90	2.69±0.58	138.45±52.16	0.66±0.23	274/240	80.00	19.33	73.97±12.05	1233.3±139.74	1.04±0.02	202/240
bn100224112	33.86	6.27±3.98	237.05±81.76	1.18±0.12	237/239	33.20	6.21	1.78±0.91	132.07±92.9	1.39±0.30	270/239
bn100322045	12.13	17.8±5.11	146.93±10.28	0.82±0.04	252/239	6.97	20.26	57.31±14.2	665.03±67.29	0.86±0.04	258/239
bn100517072	3.71	7.92±4.36	136.15±32.58	1.37±0.10	282/239	23.79	19.26	2.03±0.84	281.59±191.22	1.43±0.17	192/239
bn100615083	19.58	6.35±3.84	152.35±28.03	1.20±0.07	237/239	9.22	11.65	5.65±3.27	124.76±42.16	1.31±0.14	242/239
bn100619015	10.11	1.19±1.06	153.11±49.85	1.13±0.16	220/239	67.87	21.44	4.29±0.30	146.35±51.86	1.36±0.15	221/239
bn100709602	11.33	21.46±0.08	242.93±82.94	0.69±0.19	193/238	44.37	15.17	2.04±0.81	198.64±80.66	1.20±0.16	232/238
bn100719989	6.78	113.37±6.33	305.56±12.37	0.65±0.02	274/238	12.53	3.71	24.43±11.34	420.3±100.79	1.04±0.09	288/238
bn101023951	16.96	4.66±0.78	236.16±84.45	1.35±0.14	232/240	34.91	34.69	60.15±5.79	276.52±20.67	1.18±0.03	233/240
bn101224578	8.96	2.42±0.49	54.87±12.06	0.33±0.22	256/240	24.77	7.17	1.88±0.39	74.1±32.99	1.63±0.22	234/240
bn101231067	8.58	9.63±4.85	175.51±15.94	0.52±0.06	251/238	9.95	5.70	10.04±2.95	65.13±6.12	0.46±0.09	252/238
bn110709463	4.86	4.76±3.01	70.65±12.69	0.98±0.13	264/241	11.47	4.70	9.61±3.34	126.51±19.88	1.01±0.09	316/241
bn110717319	22.91	19.41±5.26	339.82±24.4	0.88±0.03	228/237	18.10	6.40	7.03±0.50	486.16±120.68	1.06±0.08	268/235
bn110729142	44.54	39.59±20.34	661.62±221.67	1.06±0.10	211/237	116.05	30.66	5.54±1.10	177.87±30.13	0.68±0.11	247/237
bn110824009	6.98	27.93±8.87	946.6±176.81	0.89±0.05	249/239	9.20	2.24	2.83±0.47	832.71±148.8	1.41±0.02	198/239
bn110825102	12.29	69.55±3.45	268.49±17.1	1.00±0.03	224/238	52.11	7.62	2.81±0.70	100.18±33.97	1.20±0.19	226/238
bn110903009	7.23	13.41±4.52	34.62±3.16	1.26±0.09	257/237	13.17	6.98	10.75±4.30	305.11±82.31	1.45±0.07	205/239
bn110903111	21.89	6.18±0.66	162.03±20.39	0.34±0.10	252/239	167.84	21.95	5.73±0.24	352.62±58.03	0.78±0.07	252/239
bn110904124	2.56	3.48±0.88	259.77±104.46	0.60±0.24	268/237	36.10	24.06	3.79±0.34	412.63±153.23	1.22±0.11	212/237
bn110921912	8.58	104.68±6.74	472.57±29.36	0.82±0.02	259/237	8.22	1.79	32.79±6.28	1159.32±238	1.07±0.04	232/237
bn110926107	18.62	1.74±0.49	207.54±98.64	1.30±0.15	215/238	39.24	17.09	4.52±0.38	115.31±19.91	0.96±0.10	181/238
bn111024722	16.83	8.17±4.28	139.27±18.48	0.97±0.07	220/239	32.53	19.78	1.48±0.34	48.27±11.3	0.78±0.22	205/239
bn111228657	25.28	12.04±2.16	410.98±234.65	1.94±0.08	203/237	31.07	15.10	5.32±3.34	187.16±101.4	2.19±0.10	228/236

Table 1—Continued

Trigger ID	$T_{E,I}^a$ (s)	$F_{p,I}^b$ (10^{-7} erg cm $^{-2}$ s $^{-1}$)	$E_{p,I}^c$ (keV)	α_I^d	(χ^2 /dof)	T_q^e (s)	$T_{E,II}^a$ (s)	$F_{p,II}^b$ (10^{-7} erg cm $^{-2}$ s $^{-1}$)	$E_{p,II}^c$ (keV)	α_{II}^d	(χ^2 /dof)
bn120412920	2.75	2.37±0.52	39.09±1.15	0.15±0.04	273/239	68.27	21.57	2.80±0.27	150.66±41.78	1.22±0.11	214/239
bn120530121	6.53	3.02±1.66	126.29±31.11	0.30±0.19	219/240	43.98	13.44	4.43±0.28	113.21±28.93	1.09±0.13	211/240
bn120605453	1.50	11.19±4.20	270.23±64.97	1.00±0.10	268/237	12.06	5.79	0.98±0.63	51.88±25.11	1.30±0.35	211/237
bn120618919	6.43	2.23±0.36	108.23±33.41	0.90±0.20	212/238	7.55	3.78	1.97±0.49	89.84±36.37	0.44±0.34	263/238
bn120711115	4.86	5.73±2.13	285.49±18.56	0.50±0.04	238/241	58.98	48.96	166.02±20.08	1361.46±65.98	0.98±0.01	263/239
bn120716712	6.21	0.97±0.56	126.61±43.96	0.91±0.21	246/238	170.83	35.97	4.14±0.30	153.19±21.49	1.03±0.07	247/238
bn121029350	0.45	0.17±0.24	105.35±7.12	0.33±0.07	270/239	10.80	3.95	8.58±0.25	119.23±11.33	0.39±0.09	273/237
bn121031949	9.41	5.90±0.43	257.03±74.37	0.67±0.16	237/239	182.40	12.35	1.45±0.45	209.17±82.21	1.06±0.16	230/239
bn121113544	16.90	9.58±8.66	277.2±50.58	0.77±0.08	228/238	24.45	31.94	4.84±0.36	120.75±36.2	0.88±0.17	230/238
bn121118576	12.35	14.52±3.95	228.95±56.84	1.10±0.08	237/238	8.89	13.57	1.06±0.48	102.95±45.91	1.36±0.20	233/238
bn121122870	27.01	3.37±0.12	242.77±59.87	1.22±0.08	238/237	92.88	7.74	2.82±0.33	99.11±21.35	0.68±0.15	241/237
bn121225417	27.20	40.50±6.18	458.56±40.23	0.95±0.03	224/239	19.09	28.86	24.14±4.19	287.27±30.52	1.22±0.03	197/239
bn130106995	13.50	5.61±0.84	190.28±50.68	1.25±0.11	257/239	21.57	35.01	6.80±6.32	133.63±28.99	1.51±0.09	187/239
bn130121835	24.26	18.86±5.74	164.9±13.73	0.68±0.05	227/238	130.90	32.32	1.78±0.74	184.51±91.3	1.24±0.21	216/238
bn130219775	1.79	9.05±5.30	236.69±64.47	1.00±0.13	267/238	70.58	26.05	23.90±4.88	638.77±126.38	1.13±0.06	238/238
bn130320560	16.70	1.25±0.19	212.73±198.78	1.61±0.22	201/238	141.34	53.44	6.47±6.47	281.2±111.44	1.27±0.10	188/238
bn130522510	2.03	4.80±0.15	222.38±144.44	1.59±0.19	290/237	10.30	7.46	3.43±3.39	70.36±16.63	1.11±0.16	270/238
bn130530719	11.52	1.98±0.55	100.81±19.88	0.83±0.14	249/237	38.54	9.98	1.72±0.55	347.79±439.28	1.99±0.19	249/237
bn130609902	30.08	34.17±6.55	408.22±29.61	0.70±0.03	235/239	144.64	36.22	1.49±0.69	308.3±244.42	1.64±0.16	179/239
bn130720582	80.26	7.58±3.33	80.31±13.99	0.70±0.13	227/237	37.54	136.70	19.38±2.34	98.87±11.25	1.21±0.06	249/237
bn130815660	3.07	1.71±0.41	344.26±204.99	1.42±0.15	273/238	27.89	11.97	22.30±2.33	93.52±7.4	0.97±0.05	247/239
bn130821674	57.22	55.74±4.47	603.53±86.2	1.07±0.05	221/238	28.62	8.38	8.57±3.81	165.24±58.81	1.15±0.16	243/238
bn131108024	8.83	4.75±4.54	129.26±30.61	0.97±0.13	255/237	223.36	29.57	4.61±1.06	200.48±60.42	0.13±0.26	238/237
bn140108721	11.58	8.33±5.30	173.59±38.53	1.21±0.09	243/241	67.94	14.53	12.72±5.87	479.54±110.13	1.19±0.06	215/241
bn140110814	9.22	5.17±0.60	110.61±31	0.88±0.19	246/238	32.86	11.65	1.26±1.08	65.18±37.39	1.34±0.37	259/238
bn140304849	8.26	1.59±1.21	119.19±44.87	0.67±0.27	238/239	187.97	10.50	3.41±0.51	78.02±19.3	0.51±0.21	240/239
bn140323433	64.38	13.81±3.87	152.1±14.72	0.88±0.05	204/241	20.37	45.95	7.14±3.18	98.86±16.19	1.11±0.09	221/241
bn140406120	44.29	1.76±0.59	141.73±62.91	1.23±0.20	204/239	47.82	5.89	1.80±0.43	121.19±55.38	1.30±0.21	236/239
bn140512814	6.27	15.12±12.08	578.01±172.97	0.84±0.11	274/238	94.24	44.99	12.01±8.56	992.34±347.95	1.16±0.07	204/240
bn140810782	53.06	44.06±5.02	341.54±34.04	0.82±0.05	215/239	24.64	21.06	16.9±4.83	175.65±36.69	1.18±0.09	243/239
bn140818229	9.41	1.72±0.42	82.97±28.76	0.82±0.26	256/239	64.06	44.10	17.18±7.97	204.42±16.78	0.84±0.05	257/239
bn140824606	11.46	2.87±2.88	306.67±162.11	0.94±0.19	234/238	62.85	39.30	9.84±6.60	183.89±34.16	0.90±0.09	221/238
bn140827763	11.07	13.97±4.49	218.68±20.28	0.77±0.05	240/239	11.44	3.58	3.06±0.22	105.86±5.37	1.29±0.03	240/239
bn150118409	38.34	122.34±16.28	684.01±40.04	0.89±0.02	242/238	6.11	6.72	109.32±9.23	660.14±58.01	0.85±0.04	240/238

Table 1—Continued

Trigger ID	$T_{E,I}^a$ (s)	$F_{p,I}^b$ (10^{-7} erg cm $^{-2}$ s $^{-1}$)	$E_{p,I}^c$ (keV)	α_I^d	(χ^2 /dof)	T_q^e (s)	$T_{E,II}^a$ (s)	$F_{p,II}^b$ (10^{-7} erg cm $^{-2}$ s $^{-1}$)	$E_{p,II}^c$ (keV)	α_{II}^d	(χ^2 /dof)
bn150126868	13.25	2.22±0.81	231.91±61.61	0.84±0.13	210/239	40.42	45.76	13.6±4.85	296.76±53.17	1.23±0.05	207/237
bn150220598	38.91	21.87±4.85	323.42±78.37	1.08±0.09	210/237	103.42	20.74	4.27±0.49	249.88±87.1	1.02±0.13	203/237
bn150228981	8.06	3.67±0.88	98.05±11.24	0.05±0.13	282/239	11.87	11.46	4.84±2.61	140.23±25.12	1.30±0.08	226/239
bn150323395	11.97	7.13±5.01	93.73±13.21	0.89±0.10	242/238	10.48	36.61	4.08±0.46	131.27±23.76	1.19±0.10	177/238
bn150330828	11.46	18.03±10.41	205.78±19.87	0.40±0.07	243/241	104.98	42.69	87.1±5.10	313.04±21.55	0.95±0.03	262/238
bn150426594	4.90	1.68±1.07	80.11±29.07	0.85±0.28	276/239	8.70	4.77	24.11±5.28	193.56±26.66	1.03±0.08	266/237
bn150430015	35.33	14.67±5.30	355.55±63.01	0.94±0.06	222/239	81.09	4.86	2.04±0.55	227.07±152.04	1.28±0.22	243/239
bn150507026	23.23	12.29±7.21	182.31±34.52	0.67±0.13	228/238	34.27	3.07	3.80±0.47	127.75±54.36	0.46±0.32	268/238
bn150523396	14.78	6.43±0.65	298.87±30.86	0.31±0.08	206/241	12.74	9.02	36.04±12.74	323.9±23.21	0.47±0.05	218/241
bn150619287	14.27	4.87±4.23	628.67±204.26	1.44±0.06	225/237	28.11	15.30	8.22±2.98	669.27±255.97	1.58±0.06	217/237
bn150724782	6.53	7.48±1.04	517.58±218.46	0.89±0.16	270/232	9.90	22.40	23.73±9.28	481.49±44.53	0.64±0.05	228/237
bn150729517	6.27	2.44±0.37	262.9±129.25	1.13±0.16	237/240	16.11	14.85	19.47±9.38	532.82±91.6	0.99±0.05	248/240
bn151027166	22.78	5.85±3.09	136.37±38.58	1.16±0.13	254/240	73.63	25.47	8.42±7.03	440.95±130.76	1.27±0.07	201/240
bn151030999	11.01	6.22±0.19	239.89±44.57	0.60±0.11	238/238	74.46	49.60	17.52±3.82	323.04±32.33	1.06±0.04	224/238
bn151107851	23.04	35.16±9.91	211.92±19.04	0.46±0.07	244/237	72.35	4.80	2.60±0.28	182.73±68.43	0.85±0.20	251/237
bn151227218	4.22	13.98±3.81	259.63±45.26	1.02±0.07	237/240	16.43	24.51	40.42±4.23	474.57±39.67	1.26±0.02	287/238
bn151231443	17.09	100.15±12.87	296.34±22.6	1.04±0.04	276/236	43.65	13.57	49.77±19.26	157.72±10.61	0.74±0.06	238/236
bn160215773	19.33	4.68±0.55	410.44±173.17	1.00±0.14	212/238	88.56	32.70	81.46±14.99	633.37±60.65	0.87±0.03	248/238
bn160225809	5.95	4.63±0.26	74.11±17.21	0.31±0.25	260/237	37.97	22.72	10.74±2.83	142.91±18.91	0.94±0.08	251/237
bn160303201	13.57	9.74±0.59	312.27±120.22	1.34±0.11	231/238	11.64	13.38	12.76±5.42	143.67±16.74	1.02±0.06	249/238
bn160325291	17.34	17.98±5.39	190.66±16.89	0.65±0.05	238/238	27.49	3.71	8.59±4.61	242.7±52.58	0.87±0.10	239/238
bn160802259	6.78	119.40±4.56	258.19±11.62	0.60±0.03	295/241	8.70	4.03	17.87±2.06	152.77±12.95	0.93±0.04	284/239
bn161220605	10.69	10.64±4.25	150.26±18.5	0.79±0.07	245/236	18.55	3.90	2.17±0.66	96.85±37.02	0.82±0.26	177/236
bn170115662	5.18	1.40±0.25	89.42±29.56	0.68±0.26	283/237	80.38	15.68	1.77±0.24	192.8±79.65	1.23±0.16	236/237
bn170130510	14.98	9.21±5.53	206.56±73.27	1.17±0.14	222/237	44.06	46.34	2.44±0.76	300.03±135.92	1.20±0.15	198/238
bn170208553	13.44	6.38±0.05	545.8±170.1	1.06±0.10	214/241	24.00	11.39	8.31±4.25	144.54±16.85	0.56±0.09	228/241
bn170209048	8.06	8.73±6.02	153.71±27.37	0.88±0.10	243/237	20.14	11.07	4.63±0.30	82.85±11.42	0.77±0.10	226/237
bn170228773	8.26	2.33±0.46	300.66±114.79	1.17±0.13	275/239	10.79	6.59	2.54±0.43	557.07±213.2	1.27±0.09	261/239
bn170317666	10.62	2.95±2.57	225.14±47.72	0.49±0.16	257/238	170.18	19.58	1.26±0.75	169.24±64.35	1.18±0.17	201/238
bn170409112	53.38	52.87±1.76	796.69±42.21	0.74±0.02	314/237	16.48	25.79	1.86±0.58	49.94±9.07	0.39±0.20	224/241
bn170423719	34.82	8.59±2.81	230.34±28.89	1.36±0.04	251/239	13.02	14.40	1.25±0.60	119.23±67.05	1.33±0.26	232/239
bn170510217	32.00	25.39±6.45	412.85±37.63	0.98±0.03	235/237	71.42	32.00	1.73±0.60	362.54±184.73	1.30±0.15	197/237
bn170514180	8.77	7.19±5.33	517.55±212.53	1.30±0.09	240/238	69.50	33.86	11.53±3.71	284.34±59.86	1.57±0.05	192/238

^aDuration of the first and second emission episodes.

^bFlux of the first and second emission episodes.

^cPeak energy of CPL model fits of the first and second emission episodes.

^dThe low energy photon index of CPL model fits for the first and second emission episodes.

^eThe quiescent times that are calculated from the end of the first episode to the beginning of the second episode.

¹The parameters of the Band function fits to the second episode of GRB 150330A are $\alpha = (0.95 \pm 0.03)$, $\beta = (2.3 \pm 0.07)$, $E_p = (313 \pm 22)$, and $\chi^2 = 1.1$; and for the first episode of GRB 170409A the parameters are $\alpha = (0.74 \pm 0.02)$, $\beta = (2.67 \pm 0.11)$, $E_p = (797 \pm 42)$, and $\chi^2 = 1.32$.

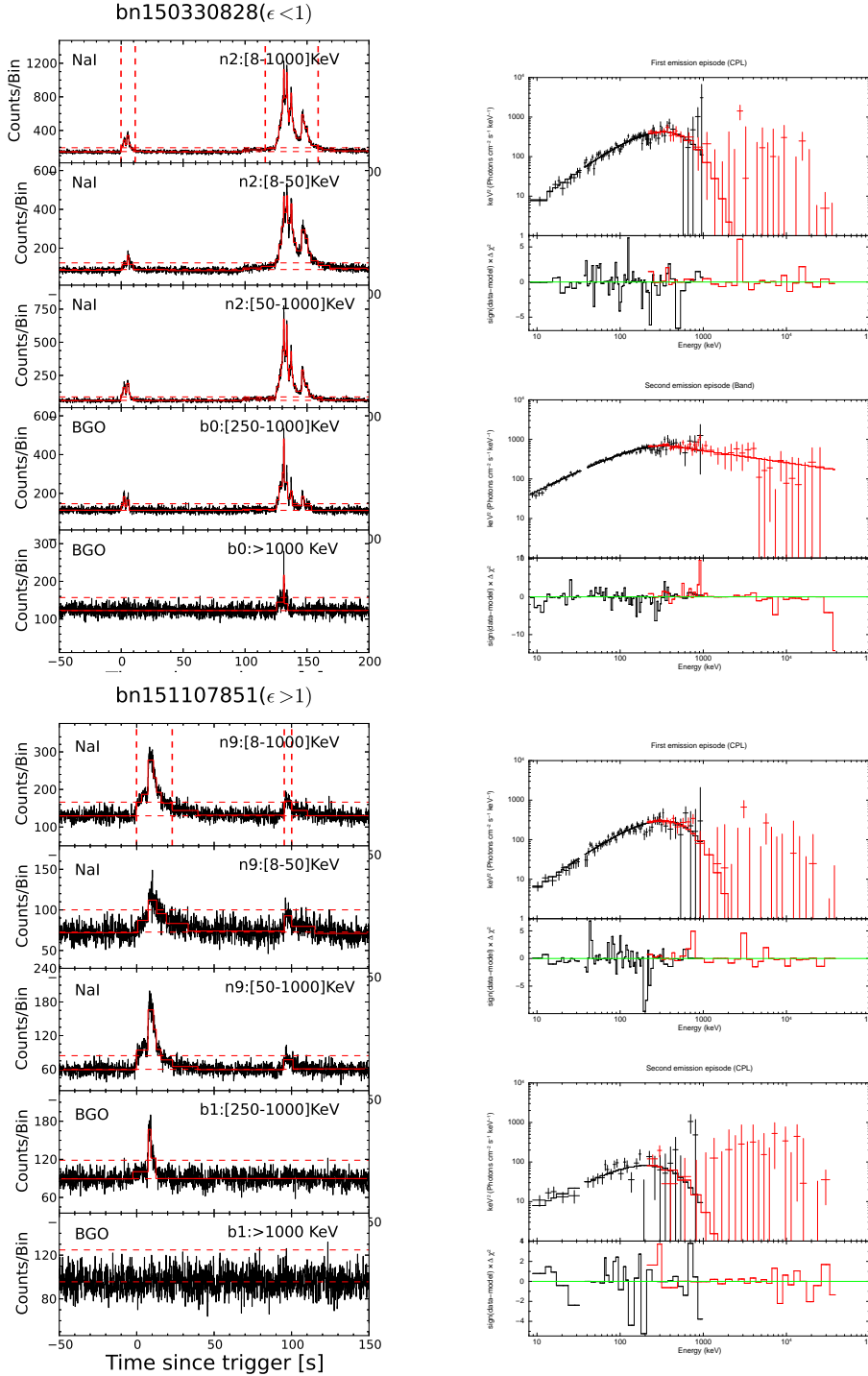


Fig. 1.— Three examples of two episodes’ emission light curves (e.g., episode I is brighter than episode II, episode II is brighter than episode I, and almost equal episodes) and spectra, together with our Bayesian block analysis (red blocks in the left panels) and spectral fits for each episode (solid line in the right panels). The dashed horizontal lines in the left panels are 3σ signal over background emission. The dashed vertical lines are the beginning and end of each emission episode.

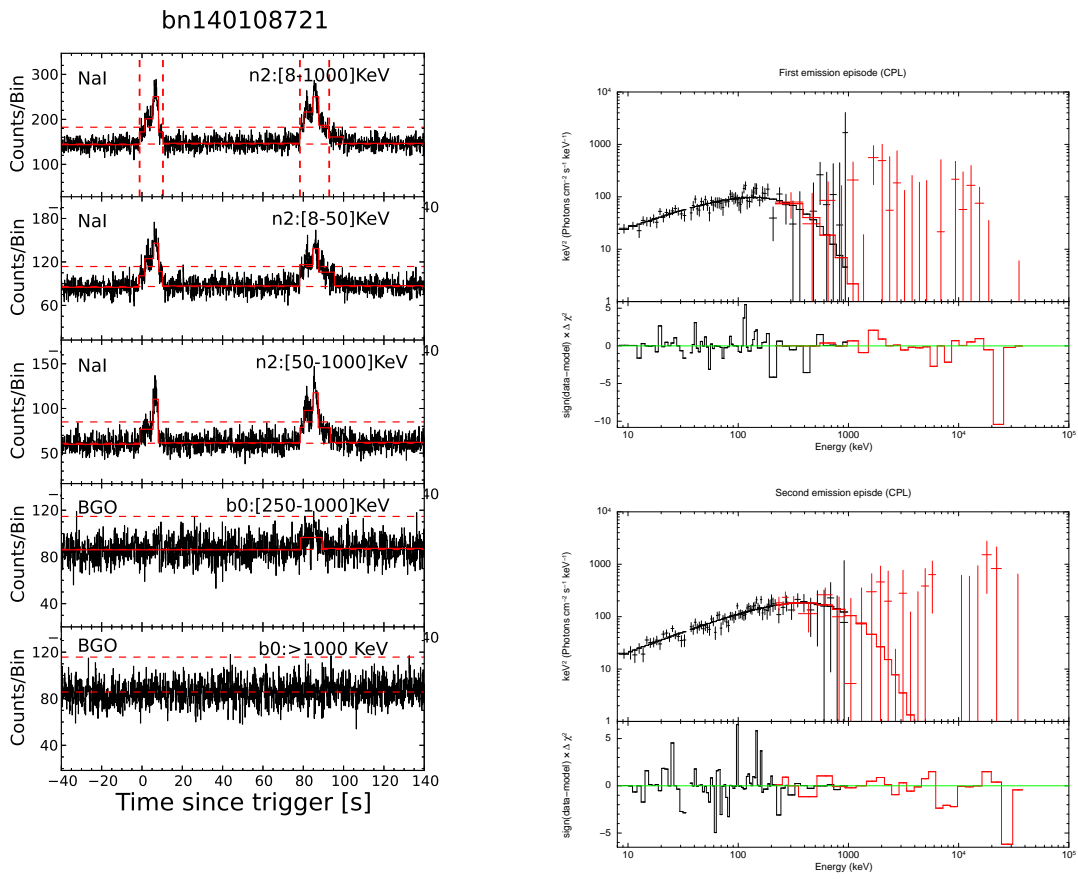


Fig. 1—Continued.

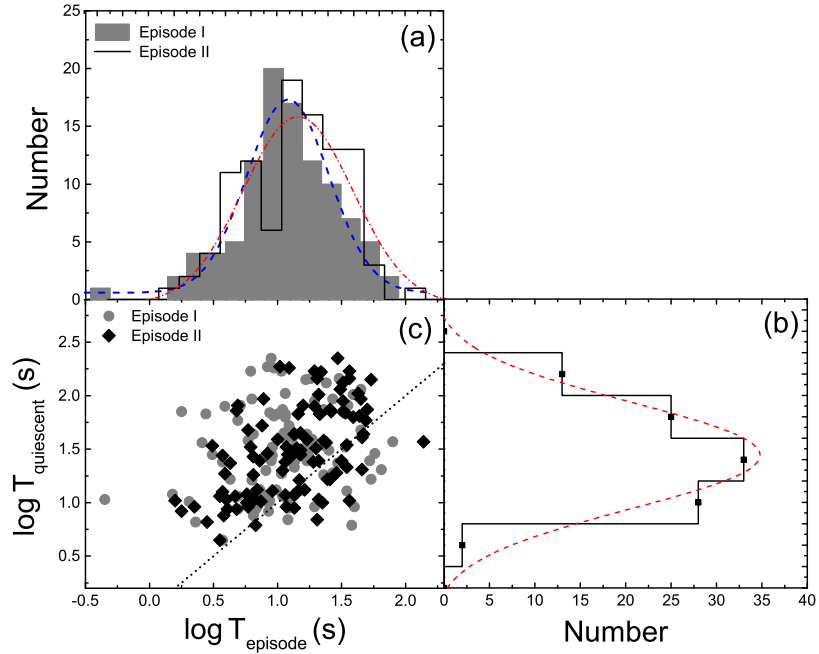


Fig. 2.— 1D and 2D distributions for the two-episode emissions in our sample in the $\log T_{\text{quiescent}}$ vs. $\log T_{\text{episode}}$. The duration distributions of the first (I) and second (II) episodes’ emission are shown in panel (a), while the duration of the quiescent time is shown in panel (b). The blue dashed line, red dashed-dotted and dashed lines are the best Gaussian fit. Panel (c) displays $T_{\text{quiescent}}$ as a function of the duration of episode I (gray dots) and II (black diamonds). The black dotted line corresponds to $T_{\text{quiescent}} = T_{\text{episode}}$.

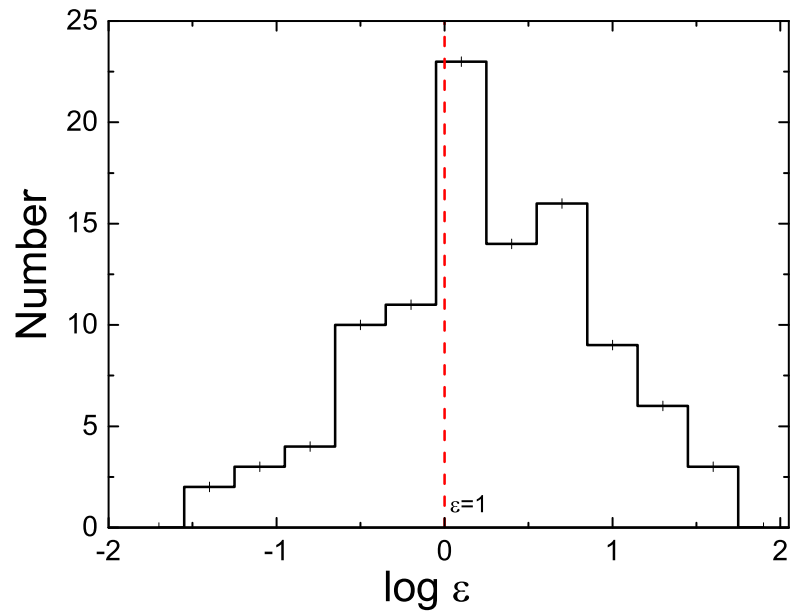


Fig. 3.— Distribution of $\log \varepsilon$ for two-episode emissions in our sample. The definition of ε is the ration of the 1 s peak flux between the first and second episodes' emission within 8 keV - 40 MeV. The dashed vertical line is $\varepsilon = 1$.

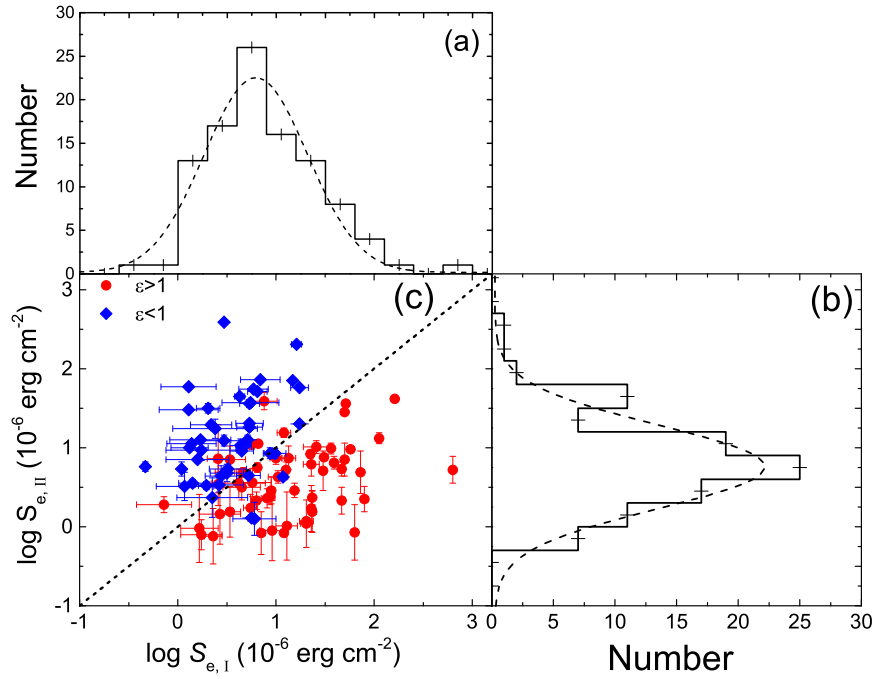


Fig. 4.— Fluence distributions of the first (I) and second (II) episodes’ emission are shown in panels (a) and (b), respectively. The dashed lines are the best Gaussian fits. Panel (c) shows the correlation of fluence for the first (I) and second (II) episodes’ emission. The dotted line is $S_{e,I} = S_{e,II}$. The blue diamonds and red points correspond to $\epsilon < 1$ and $\epsilon > 1$, respectively.

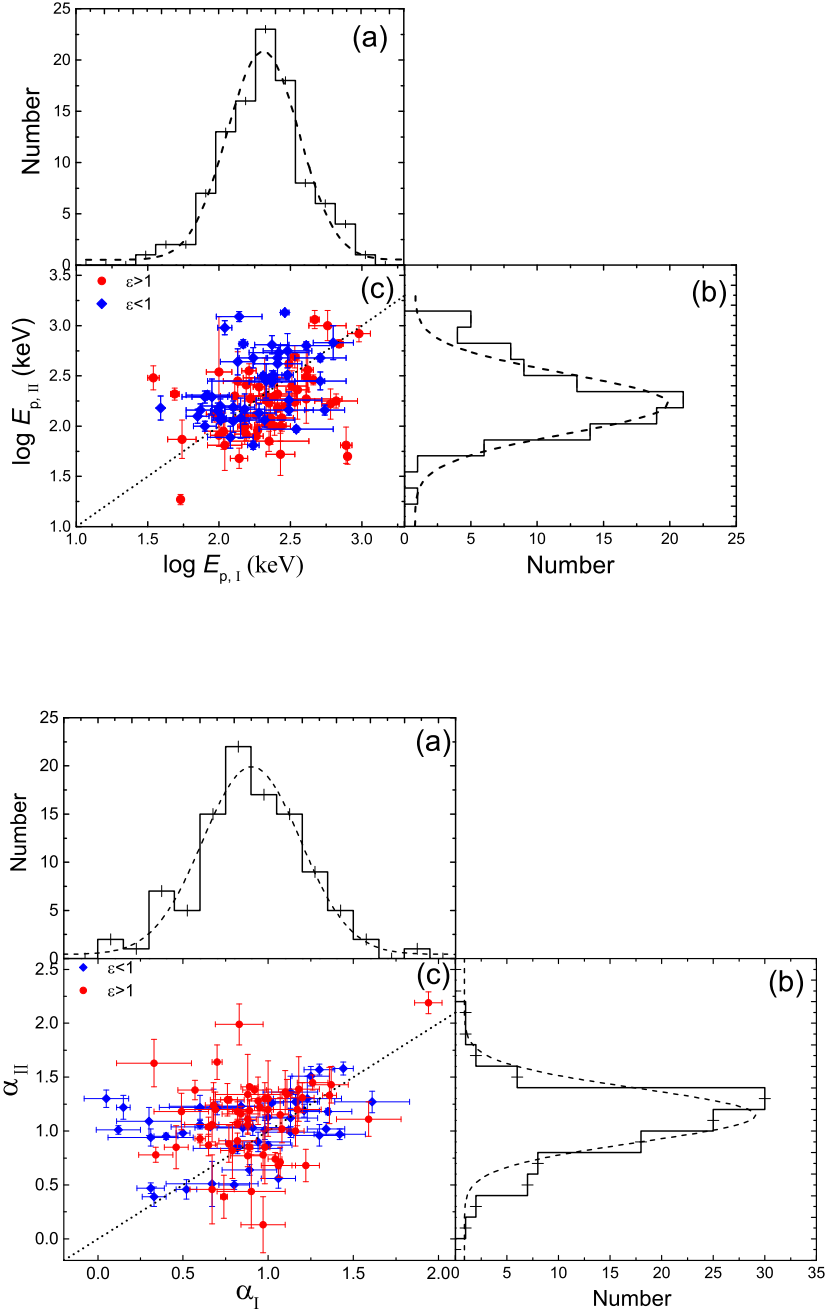


Fig. 5.— Distributions of peak energy $E_{p,I}$ and $E_{p,II}$ (top panel), photon index α_I and α_{II} (bottom panel), and their correlations for our sample. Black dashed lines are the best Gaussian fits, and black dotted lines correspond to $E_{p,I} = E_{p,II}$ (top panel) and $\alpha_I = \alpha_{II}$ (bottom panel). The red dots and blue diamonds correspond to $\varepsilon > 1$ and $\varepsilon < 1$, respectively.